Chapter 33
Evolution Through Helium Burning: Low-Mass Stars

33.1 Post-Main-Sequence Evolution

Compared to more massive stars, those of lower masses (typically $M < 2.3 M_\odot$) evolve in a qualitatively different way after the exhaustion of hydrogen in their central regions. There are several reasons for this difference. Low-mass main-sequence stars have small, or no, convective cores, and degeneracy is important, if not on the main sequence, then shortly afterwards. In addition they start at a point on the main sequence much closer to the Hayashi line than the starting points of massive stars.

For example, if hydrogen is consumed in a well-mixed convective core, there will be a helium core of appreciable mass at the very end of central hydrogen burning. However, stars of around $1 M_\odot$ have no convective cores; they consume hydrogen as illustrated in Fig. 30.1. Consequently they produce a growing helium core starting at zero mass. Therefore there is a smooth transition from central to shell burning. These stars start with such large central densities ($\gtrsim 10^2\,\mathrm{g\,cm^{-3}}$) that the electron gas is at the border of degeneracy, which has several consequences. The Schönberg–Chandrasekhar limit (Sect. 30.5) is not important: initially, the core mass M_c is below $0.1 M$. When, however, with outward burning shell source $M_\mathrm{c} > 0.1 M$, the core contraction has produced sufficient degeneracy, making this limit irrelevant. The stars can then well exist in thermal equilibrium with a degenerate, isothermal helium core. This means that there is no "need" for a *rapid* core contraction as described in Sect. 31.1 and no equivalent of the Hertzsprung gap. Another consequence of degeneracy is that core contraction is not connected with heating. This is in contrast to the pre-main-sequence contraction (Sect. 28.1) and to post-main-sequence core contraction, which leads to helium ignition in massive stars.

At least in the first phases to be discussed here, the growth of the core mass is slow (since the productivity of the shell source is low), and the whole core settles at the temperature of the surrounding hydrogen-burning shell. This means that the core temperature is far from that of the ignition of helium ($\approx 10^8$ K). In low-mass stars, helium burning will be seen to start much later owing to secondary effects, after

R. Kippenhahn et al., *Stellar Structure and Evolution*, Astronomy and Astrophysics Library, DOI 10.1007/978-3-642-30304-3_33, © Springer-Verlag Berlin Heidelberg 2012

the core mass has grown up to a certain limit. Therefore the shell-burning phase between the central hydrogen and helium burning is a nuclear, slow phase, and one can expect to find many such stars in the sky.

The contraction of the core is (as in the case of larger M) accompanied by an expansion of the hydrogen-rich envelope outside the shell source. However, as long as the luminosity does not change drastically, the expansion cannot carry the star far away from its starting point on the main sequence. The reason is that this point is already close to the Hayashi line, which cannot be crossed (Chap. 24).

Any further expansion of the envelope is only possible if the luminosity increases. In fact the calculations show that L now increases by more than a factor 10^2 while M_c grows.

Surprisingly enough it turns out that L soon depends on the properties of the core only and is practically independent of the mass of the envelope (and therefore of M). In this phase the models can be well described analytically by a generalized form of homology.

33.2 Shell-Source Homology

Consider a model in complete equilibrium consisting of a degenerate helium core (mass M_c, radius R_c) surrounded by an extended envelope of hydrogen with abundance X_H and mass $M_{env} = M - M_c$. The core mass M_c grows owing to hydrogen-shell burning, which provides the luminosity L:

$$\dot{M}_c = \frac{L}{X_H E_H} \tag{33.1}$$

(where E_H is the energy gain per unit mass of hydrogen). This equation could easily be integrated if L were constant. However, while evolution proceeds, L grows too since there is a relation between L and M_c. The properties of the shell (and therefore L) are mainly determined by M_c and R_c, while they are almost independent of the properties of the envelope. This can be understood from the fact that the core is highly concentrated and the gravity at its surface is very large. Then, according to hydrostatic equilibrium, $|dP/dm| \sim m/r^4$ is very large, and P drops by powers of 10 within a thin mass shell just above the core surface. The typical situation is illustrated in Fig. 33.1. In other words, the extended envelope above this layer is nearly weightless and has no influence on the burning shell.

We now present an analytic approach of Refsdal and Weigert (1970) giving relations between the properties of the core and the physical variables in the hydrogen-burning shell. For this purpose we will generalize the homology considerations of Chap. 20 and use again the power approximations for κ and ε:

$$\kappa = \kappa_0 P^a T^b, \quad \varepsilon = \varepsilon_0 \varrho^{n-1} T^\nu. \tag{33.2}$$

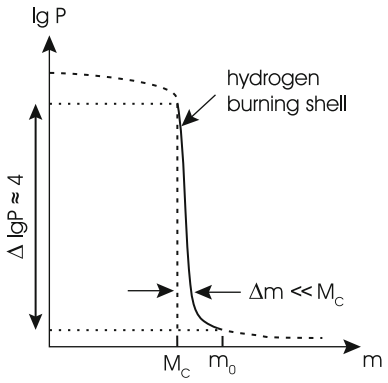

Fig. 33.1 A schematic sketch of the run of pressure in the vicinity of a thin shell. M_c is the mass of the core; the shell extends to $M_0(r_0)$. Its thickness is Δr, i.e. $M_0 = M_r(R_c + \Delta r)$ (After H. Ritter, priv. communication)

Here we have replaced the exponent λ used in Chap. 20 by $n - 1$.

For the gas pressure we will use the ideal-gas equation

$$P = \frac{\Re}{\mu}\varrho T \ , \tag{33.3}$$

since we only want to apply it to regions outside the core, where the gas is not degenerate. We also neglect radiation pressure since it is not important for low-mass stars. In Chap. 35 we shall apply the relations derived here to more massive stars and then take radiation pressure into account.

We now assume for the density, temperature, pressure, and local luminosity in the region of the hydrogen-burning shell (i.e. for $R_c \le r \le R_c + \Delta r$) that there exists a simple dependency on M_c and R_c:

$$\varrho(r/R_c) \sim M_c^{\varphi_1} R_c^{\varphi_2} \ , \tag{33.4}$$

$$T(r/R_c) \sim M_c^{\psi_1} R_c^{\psi_2} \ , \tag{33.5}$$

$$P(r/R_c) \sim M_c^{\tau_1} R_c^{\tau_2} \ , \tag{33.6}$$

$$l(r/R_c) \sim M_c^{\sigma_1} R_c^{\sigma_2} \ . \tag{33.7}$$

These homology-type relations have the following meaning: we compare two stellar models of different core masses M_c and M_c' and core radii R_c and R_c'. We define homologous points, r and r', in the two models by

$$\frac{r}{R_c} = \frac{r'}{R_c'} \ ; \tag{33.8}$$

the physical quantities at homologous points in the two models shall then be connected by relations (33.4)–(33.7). This indeed is very similar to the considerations of Sect. 20.1, though there the homologous points were defined with respect to the total radius R, whereas we here define them with respect to the core radius R_c.

While there, for example, in (20.9), the physical quantities vary like powers of M and R, they here vary like powers of M_c and R_c. For example, with our new concept of homology, (20.9) is replaced by (33.4) and (33.6), which are written explicitly as

$$\frac{\varrho}{\varrho'} = \left(\frac{M_c}{M_c'}\right)^{\varphi_1} \left(\frac{R_c}{R_c'}\right)^{\varphi_2} , \tag{33.9}$$

$$\frac{P}{P'} = \left(\frac{M_c}{M_c'}\right)^{\tau_1} \left(\frac{R_c}{R_c'}\right)^{\tau_2} . \tag{33.10}$$

We now introduce relations (33.4)–(33.7) into the stellar-structure equations in order to determine the exponents. We therefore write (2.4), (5.11), and (4.42) in the form

$$dP \sim M_c \varrho d(1/r) , \tag{33.11}$$

$$d(T^4) \sim \kappa \varrho l \, d(1/r) = \kappa_0 \varrho P^a T^b l \, d(1/r) , \tag{33.12}$$

$$dl \sim \varepsilon \varrho d(r^3) = \varepsilon_0 \varrho^n T^\nu d(r^3) , \tag{33.13}$$

with positive factors of proportionality. In (33.11) we have assumed that $m \approx M_c$ = constant, which is a sufficient approximation in the region in which P drops to negligible values. This assumption yields decisive differences from the relations discussed in Chap. 20. Introducing (33.4)–(33.6) into (33.3) we easily obtain for the exponents

$$\tau_1 = \varphi_1 + \psi_1, \quad \tau_2 = \varphi_2 + \psi_2 . \tag{33.14}$$

We now integrate (33.11)–(33.13) over the shell, starting with (33.11): we choose a radius r_0 sufficiently larger than R_c that $P(r_0/R_c) \ll P(r/R_c)$, and find from (33.11) that

$$P(r/R_c) = P(r_0/R_c) + \int_{1/r_0}^{1/r} GM_c \varrho d(1/r) \approx \frac{GM_c}{R_c} \int_{x_0}^{x} \varrho \, dx , \tag{33.15}$$

with $x = R_c/r$. If we do the same for another model with M_c', R_c', we find for the pressure at the homologous radius r'

$$P'(r'/R_c') \approx \frac{GM_c'}{R_c'} \int_{x_0}^{x} \varrho' \, dx = \frac{GM_c'}{R_c'} \left(\frac{M_c'}{M_c}\right)^{\varphi_1} \left(\frac{R_c'}{R_c}\right)^{\varphi_2} \int_{x_0}^{x} \varrho \, dx , \tag{33.16}$$

where (33.9) has been introduced into the integral. Comparing (33.16) with (33.15) yields

$$P(r/R_c) \sim M_c^{\varphi_1+1} R_c^{\varphi_2-1} , \tag{33.17}$$

and if we compare this with (33.6) we find

$$\tau_1 = \varphi_1 + 1, \quad \tau_2 = \varphi_2 - 1 . \tag{33.18}$$

The same procedure can be carried out using (33.12) and (33.13). For the integration in the first case we again choose r_0 sufficiently far outside, where the temperature is small compared to its values in the shell; for the integration of (33.13) we take $r_0 = R_c$, where the local luminosity vanishes. We then obtain

$$(4-b)\psi_1 = \varphi_1 + a\tau_1 + \sigma_1 \,, \tag{33.19}$$

$$(4-b)\psi_2 = \varphi_2 + a\tau_2 + \sigma_2 - 1 \,, \tag{33.20}$$

$$\sigma_1 = n\varphi_1 + \nu\psi_1, \quad \sigma_2 = n\varphi_2 + \nu\psi_2 + 3 \,. \tag{33.21}$$

Equations (33.14) and (33.18)–(33.21) are eight linear inhomogeneous algebraic equations for the eight exponents in (33.4)–(33.7). The solutions are

$$\begin{aligned} &\varphi_1 = -\frac{\nu - 4 + a + b}{N}, \quad \varphi_2 = \frac{\nu - 6 + a + b}{N}, \quad \psi_1 = 1, \quad \psi_2 = -1 \,, \\ &\tau_1 = 1 + \varphi_1, \quad \tau_2 = \varphi_2 - 1, \quad \sigma_1 = \nu + n\varphi_1, \quad \sigma_2 = 3 - \nu + n\varphi_2 \,, \end{aligned} \tag{33.22}$$

with

$$N = 1 + n + a \,. \tag{33.23}$$

Equations (33.22) allow us to determine the variations of the physical quantities from one model (characterized by M_c, R_c) to another (characterized by M_c', R_c'). The temperature and the local luminosity at homologous points vary as

$$T \sim M_c^{\psi_1} R_c^{\psi_2} = M_c/R_c \,, \tag{33.24}$$

$$l \sim M_c^{\nu+n\varphi_1} R_c^{3-\nu+n\varphi_2} \,. \tag{33.25}$$

This holds for all homologous points, also for those at the upper border of the range of integration where $l = L$. Therefore the luminosity of these shell-source models depends on M_c (rather than on M) and on the mode of energy generation (in striking contrast to main-sequence type models, cf. Chap. 20). As an illustration we assume $a = b = 0$ (electron scattering, see Sect. 17.1) and $\nu = 13, n = 2$ (CNO cycle, see Sect. 18.5.1). Then $\varphi_1 = -3, \varphi_2 = 7/3$, and we find

$$L \sim M_c^7 R_c^{-16/3} \,. \tag{33.26}$$

We have obtained relations $T(M_c, R_c)$ and $L(M_c, R_c)$ independent of M. In order to see how T and L vary along an evolutionary sequence of models with increasing M_c, one has to know how R_c varies with M_c. Since the cores in the evolution under consideration are degenerate, they resemble white dwarfs whose radii decrease with increasing mass (see Sect. 19.6, Chap. 37). We therefore can expect from (33.24) that the temperature in the shell source increases with M_c, and according to (33.26), the luminosity increases strongly with M_c even with R_c = constant (this increase being much steeper than the $L(M)$ relation for main-sequence stars).

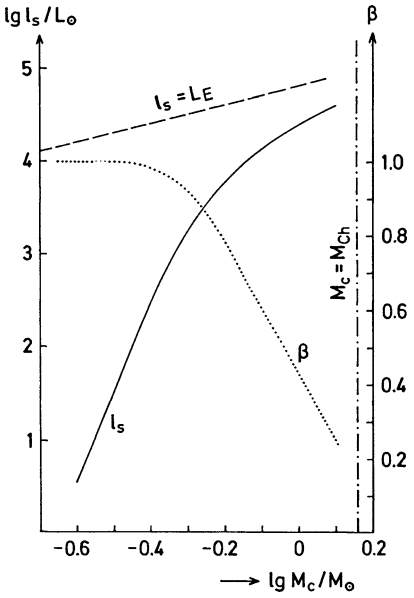

Fig. 33.2 The luminosity l_s (*solid curve, left ordinate*) at the top of the hydrogen-burning shell around a degenerate helium core of mass M_c. The *dotted line* indicates the importance of the radiation pressure, the value of $\beta(= P_{gas}/P_{total})$ being given by the ordinate at the *right*. When M_c approaches the Chandrasekhar mass M_{Ch} (Sect. 19.7; *dot-dashed vertical line*), the luminosity curve has the tendency to approach the Eddington luminosity L_E (*dashed line*) for which gravity equals the radiation-pressure gradient (for an opacity dominated by electron scattering; see Sect. 22.5)

We now need a relation $R_c(M_c)$. The classical mass-radius relation for white dwarfs (Chap. 37) is, of course, not directly applicable to these cores. Below the shell there must be a transition from complete through partial to no degeneracy. Compared to the outer layers of white dwarfs, this transition region is very hot (like the shell source) and may occupy an appreciable fraction of the core volume (For a discussion of this problem, see Refsdal and Weigert 1970.). Nevertheless, as a simple example for $R_c(M_c)$ we here take the relation for the cold white dwarfs of Table 37.1, yielding $d\ln R_c/d\ln M_c$ for different values of M_c. This can be used in

$$\frac{d\ln L}{d\ln M_c} = \sigma_1 + \sigma_2 \frac{d\ln R_c}{d\ln M_c}\,, \tag{33.27}$$

which follows from (33.7). The coefficients σ_1 and σ_2 are determined by (33.22). For $a = b = 0, n = 2, \nu = 14$, one finds $d\ln L/d\ln M_c \approx 8\cdots10$. We can also integrate (33.27) numerically when starting from a correctly computed model, which gives an initial value L for a given M_c. The results of such an integration, l_s, are shown in Fig. 33.2 by the left part of the solid curve where radiation pressure can be neglected ($\beta \approx 1$).

For the temperature at homologous points, say at the bottom of the hydrogen-burning shell, instead of (33.27), we obtain from (33.24)

$$\frac{d\ln T}{d\ln M_c} = 1 - \frac{d\ln R_c}{d\ln M_c}\,, \tag{33.28}$$

and we get $d\ln T/d\ln M_c$ somewhat larger than 1. Since the cores are assumed to be isothermal, this also gives the increase of the central temperature T_c. We see that in this way T_c can be raised to helium ignition even by models in complete equilibrium.

33.3 Evolution Along the Red Giant Branch

In the following we describe the evolution of a star of $1.3\,M_\odot$ as calculated by Thomas (1967) in a pioneering paper. The chemical composition of the initial model on the ZAMS is $X_H = 0.9$, $X_{He} = 0.099$, $Z = 0.001$, which at that time seemed to be the appropriate mixture for a star of population II. The essential results, however, do not depend too much on the chosen chemical composition, as we will show later and in Fig. 33.5. The initial model has $L = 1.91\,L_\odot$, $T_{eff} = 6,760\,\mathrm{K}$. Nuclear energy is released in the central region at $T_c = 1.48 \times 10^7\,\mathrm{K}$. There is a small convective core containing 4.3 % of the total mass, which disappears long before the exhaustion of hydrogen in the centre. There is also an outer convective zone, which reaches inwards from the photosphere to about $r \approx 0.95R$.

The evolutionary track in the HR diagram is shown in Fig. 33.3, while the internal evolution is illustrated by Fig. 33.4. In the HR diagram the image point of the model first moves upwards and then to the right. At the same time, the model switches from central nuclear burning to shell burning, as can be seen in Fig. 33.4. We have already learned from the shell-source homology of Sect. 33.2 that the luminosity must grow with increasing core mass. The calculated evolution confirms these predictions once the core is sufficiently compressed. The track is very close to the Hayashi line, leading up along the giant branch to higher luminosities and correspondingly larger radii. The neighbourhood of the line of fully convective stars can also be seen from the internal structure of the models. Figure 33.4 shows that the outer convective zone penetrates deeply inwards until more than 70 % of the total mass is convective. It then reaches into layers which are already contaminated by products of nuclear reactions (see dotted area in Fig. 33.4). The processed material is distributed over the whole convective region and therefore also brought to the surface. This type of partial mixing, the *first dredge-up*, we have already encountered for more massive stars in Chap. 31.

The monotonic increase of the luminosity is interrupted when the hydrogen-burning shell reaches the layer down to which the outer convective zone has mixed at the moment of deepest penetration. At this point the mixing has produced a discontinuity in molecular weight between the homogeneous hydrogen-rich outer layer and the helium-enriched layers below. When the shell source reaches the

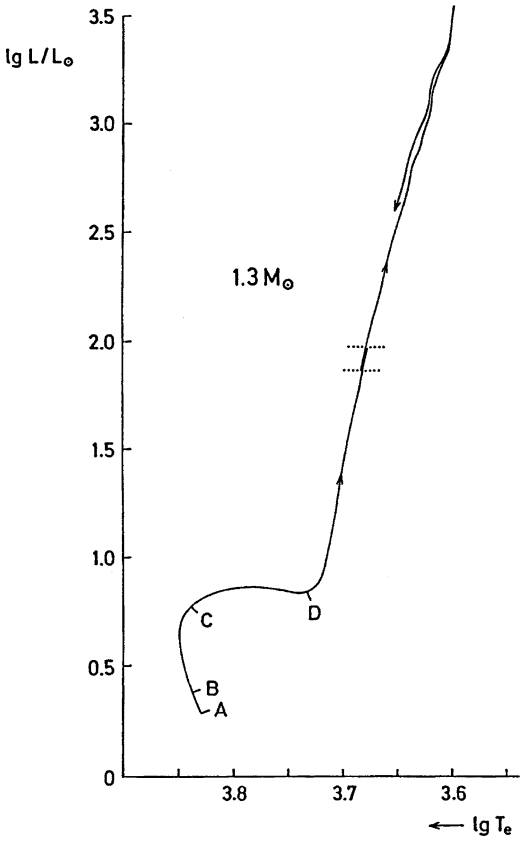

Fig. 33.3 The evolutionary track of a star of $1.3M_\odot$ with the initial composition $X_\mathrm{H} = 0.9$, $X_\mathrm{He} = 0.099$, $Z = 1 - X_\mathrm{H} - X_\mathrm{He} = 0.001$ as computed by Thomas (1967). The letters $A - D$ refer to the corresponding evolutionary states in Fig. 33.4. The *arrows* indicate the direction of the evolution. This direction is reversed for a short period between the *dotted horizontal lines*. This transient drop in luminosity at about $\lg L/L_\odot = 2$ occurs when the hydrogen-burning shell crosses the chemical discontinuity left behind when the bottom of the outer convective zone moves outwards again in the mass scale after it has reached its deepest extension (see Fig. 33.4)

discontinuity, the molecular weight of the shell material becomes smaller. This causes the drop of luminosity at $L \approx 100L_\odot$ (see Fig. 33.3) as can easily be understood.

For this purpose we follow the considerations of Sect. 33.2, but this time, we vary the molecular weight μ at homologous points while keeping M_c, R_c, and all other parameters constant. Analogously to (33.4)–(33.7) we write

$$\varrho(r/R_\mathrm{c}) \sim \mu^{\varphi_3} \,, \tag{33.29}$$

$$T(r/R_\mathrm{c}) \sim \mu^{\psi_3} \,, \tag{33.30}$$

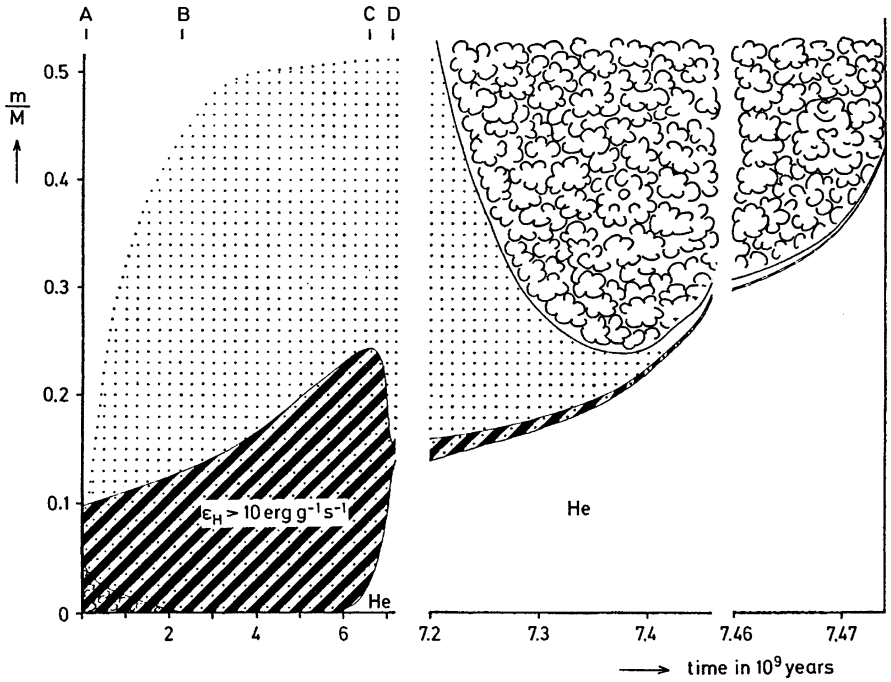

Fig. 33.4 The evolution of the internal structure of a star of $1.3M_\odot$ plotted in the same manner as in Fig. 31.2a. The main region of hydrogen burning is hatched; "cloudy" areas indicate convection. Regions of variable hydrogen content are *dotted* (After Thomas 1967)

$$P(r/R_c) \sim \mu^{\tau_3} \,, \tag{33.31}$$

$$l(r/R_c) \sim \mu^{\sigma_3} \,, \tag{33.32}$$

and with the same procedure as in Sect. 33.2 we find

$$\varphi_3 = \frac{4-b-\nu}{N}, \quad \psi_3 = 1, \quad \tau_3 = \varphi_3, \quad \sigma_3 = \nu + n\varphi_3 \,, \tag{33.33}$$

with $N = 1+n+a$. For example, using again the values $\nu = 13, n = 2, a = b = 0$ as in Sect. 33.2, we see that (33.32) becomes $l \sim \mu^7$. Therefore the luminosity decreases with decreasing μ, which explains the transient reduction of L. After the shell source has passed the discontinuity, μ remains at its reduced value and the luminosity grows again with increasing core mass. As the star passes three times through the region between the two dotted horizontal lines in Fig. 33.3, observations have a higher probability of finding stars in this luminosity range than in the neighbouring ones. In luminosity functions of globular clusters, which give the number of stars per brightness bin, this event in the evolution of low-mass stars shows up as a localized peak, which is either called *Thomas peak*, or simply

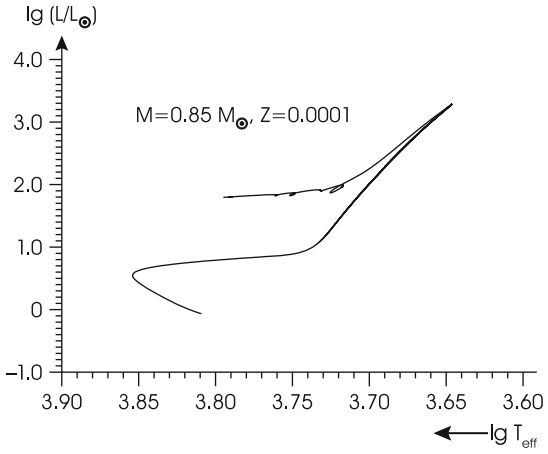

Fig. 33.5 The evolutionary track of a star of 0.85 $M_\odot$ and composition $X_\mathrm{H} = 0.7499$, $X_\mathrm{He} = 0.25$, and $Z = 0.0001$. This is the modern version of Fig. 33.3 calculated with a modern stellar evolution code and a Pop. II composition typical for metal-poor globular clusters. The evolution proceeds from the main sequence to the tip of the red giant branch at $\log L/L_\odot \approx 3.2$, through the helium flash to the horizontal branch

the *bump*. Indeed, in high-quality photometry of clusters, it can be found easily. As an example, we refer the reader to the case of NGC 5824 (Zoccali et al. 1999).

Evolutionary calculations for somewhat different total masses M yield similar results. Near the main sequence the tracks are shifted relative to each other according to their different starting points on the ZAMS. When approaching the Hayashi line the tracks merge (This is not exactly true, since different total masses have slightly different Hayashi lines.). After the cores are sufficiently condensed they are virtually independent of the envelope (and therefore of the total mass M). However, they determine the total luminosity according to the $L(M_\mathrm{c})$ relation. Consequently stars of different M but the same M_c have the same L and are practically at the same point in the HR diagram.

The same convergence of the evolution for different M must occur for all properties of the shell source and the core. For example, the central values of density and temperature converge to the same evolutionary track in the ϱ_c–T_c plane.

Numerical calculations show that with growing core mass the temperature in the core rises. This is due to two effects which are of approximately the same order. The first is the increase of the temperature in the surrounding shell source where $T \sim M_\mathrm{c}/R_\mathrm{c}$ after (33.24). While this effect already occurs in models of complete equilibrium, there is an additional effect due to non-stationary terms. With growing M_c the core contracts, releasing energy. If this occurs rapidly enough, it heats up the transition layer below the shell, and therefore the whole core. An inward-directed temperature gradient is built up in the transition region, such that the energy released by ε_g terms is carried away. However, this is not the whole story, since at the same time conditions in the core are such that cooling by plasma neutrinos, which were

discussed in Sect. 18.7 (see also Fig. 18.11), becomes important and modifies the temperature gradient, as will be seen in Sect. 33.5. The core evolution is enhanced by increasing L: the rate $\dot{M}_c$ is proportional to L, which in turn increases by a high power of M_c, and the process speeds up more and more. Both these effects, controlled by the growth of M_c, finally increase the core temperature to $\approx 10^8$ K at which helium is ignited. This happens when $M_c \approx 0.48 M_\odot$, almost independently of M, but slightly decreasing with increasing metallicity. The matter in the core is highly degenerate, and the nuclear burning is unstable. The resulting thermal runaway terminates the slow and quiet evolution along the giant branch.

33.4 The Helium Flash

We start with some analytic considerations and assume that helium is ignited in the centre, where the electron gas is assumed to be non-relativistic and degenerate. In Sect. 25.3.5 we have discussed the secular stability of nuclear burning in a small central sphere of mass m_s, "luminosity" $l_s = \varepsilon m_s$, and gravothermal specific heat c^*. Assuming a homologous reaction of the layers above, a small relative temperature perturbation $\vartheta_c (= dT_c/T_c)$ was shown in (25.35) to evolve according to

$$\dot{\vartheta}_c = \frac{l_s}{c_P m_s T_c} (\varepsilon_T + \kappa_T - 4) \vartheta_c \,, \tag{33.34}$$

where we have set $\delta = 0$ and therefore $c^* = c_P$ according to (25.29). For helium burning we have $\varepsilon_T > 19$ (see Sect. 18.5.2), which certainly dominates the other terms in the parenthesis which thus is positive: the onset of helium burning in the degenerate core is unstable and results in a thermal runaway. The timescale of the thermal runaway is of the order $c_P m_s T_c / l_s = c_P T_c / \varepsilon$, i.e. of the order of the thermal timescale of the helium-burning region.

The homologous linear approximation which yielded (33.34) can only give a very rough picture of the events after helium ignition. Nevertheless we can try to discuss the consequences which follow from our simple formalism. From (25.25) and (25.26) one obtains

$$\frac{d\varrho_c}{\varrho_c} = \frac{3\delta}{4\alpha - 3} \vartheta_c \,, \tag{33.35}$$

and for the completely degenerate non-relativistic gas, where $\alpha = 3/5, \delta = 0$, we find $d\varrho_c = 0$. Therefore, while during the thermal runaway the central temperature is rising, the matter neither expands nor contracts. The central density remains constant, and in the $\lg \varrho_c$–$\lg T_c$ diagram, the centre evolves vertically upwards as indicated in Fig. 33.6. The reason is that in the (fully) degenerate gas the pressure does not depend on temperature and therefore remains constant during the thermal runaway. But only an increase of pressure could lift the weight of the mass above and cause an expansion. Since the $P dv$ work is zero, all nuclear power goes into internal energy. During the thermal runaway there is an enormous overproduction of nuclear energy. The local luminosity l at maximum comes to $10^{11} L_\odot$, about that of

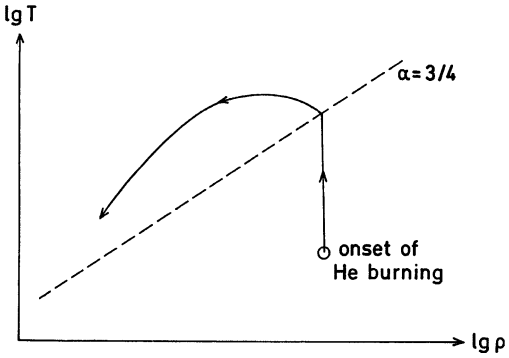

Fig. 33.6 Schematic sketch of the changes of temperature and density during the helium flash. After the ignition temperature is reached in the regime of degeneracy the temperature rises almost without a change of density until degeneracy is removed near the *broken line*. Then a phase of almost isothermal expansion ensuesfollowed by a phase of stable helium burning in the non-degenerate regime

a whole galaxy, but only for a few seconds (The expression "helium flash" is quite appropriate indeed!). However, almost nothing of it reaches the surface, since it is absorbed by expansion of the non-degenerate layers above.

With increasing temperature at constant density, the degeneracy is finally removed. This happens roughly when in Fig. 33.6 the border ($\alpha = 3/4$) between degeneracy and ideal gas is crossed. Then with further increase of T the core expands. With the removal of degeneracy the gravothermal specific heat becomes negative again and central helium burning becomes stable; the expansion stops the increase of temperature. The overproduction then is gradually removed by cooling until the temperature has dropped to "normal" values for quiet (stable) helium burning. In the $\lg \varrho_c$–$\lg T_c$ plane the core settles near the image point of a homogeneous helium star of mass M_c, which is of the order of $0.48 M_\odot$.

There is another prediction we can make for the changes in the HR diagram. Until the onset of helium burning the total luminosity of the star (which is just the power produced in the shell) increases with increasing core mass as expected from (33.26). After degeneracy is removed in the central region, the core expands and R_c increases. During the short phase of the flash, M_c remains practically unchanged. From (33.26) we therefore expect the luminosity to be appreciably reduced after the flash phase, and this indeed can be seen from Figs. 33.3 and 33.5.

33.5 Numerical Results for the Helium Flash

In Sect. 33.4 we have tacitly assumed that the maximum temperature is in the centre. This, however, is not the case if neutrinos–as we discussed them in Sect. 18.7–are created in the very interior of the core and provide an energy sink there, since they

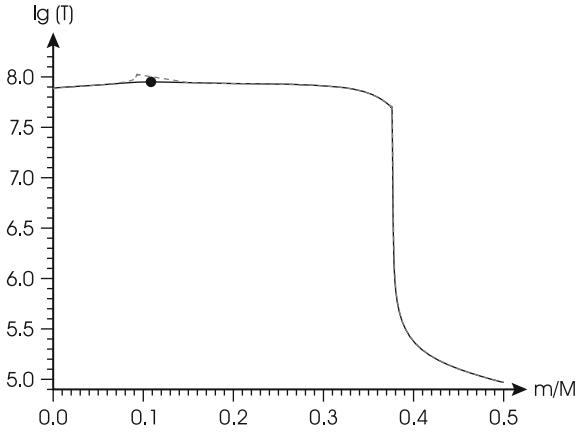

Fig. 33.7 The temperature T (in K) as a function of the mass variable m in a $1.2M_{\odot}$ model with solar metallicity, shortly before the onset of (unstable) helium burning (*solid line*). Owing to neutrino losses the maximum temperature does not occur in the centre but near $m/M = 0.1$ (indicated by the *dot*). The *dashed line* (deviating from the *solid* one only near the *dot*) shows how the ignition of helium burning has raised the temperature at this position inside the star only 10^4 years later

leave the star without noticeable interaction. Then the maximum of temperature is not in the centre but at a finite value of m (see Fig. 33.7). From there, energy flows outwards ($l > 0$) and inwards ($l < 0$). This energy is released by core contraction in the transition zone below the burning shell as mentioned in Sect. 33.3. The transport mechanisms are radiation and conduction. The inward-going energy is carried away by neutrinos. Then the ignition of helium and the flash will not take place in the centre but in the concentric shell of maximum temperature. This is near $m/M = 0.1$ according to Fig. 33.7 [Note that in the calculations shown in Fig. 33.4 an unusually low value of μ in the envelope was assumed. Therefore, according to (33.30) and (33.32), T in the shell source and L are smaller for the same M_c and R_c, and helium ignites at correspondingly larger M_c, in this case at $m/M \approx 0.3$, cf. Fig. 33.10.].

In Fig. 33.8, the evolution is shown in a lg ϱ–lg T diagram for the shell in which helium is ignited. We see that the shell behaves roughly as predicted in Fig. 33.6 for the centre. When the temperature of helium burning is reached at point A, the core matter heats up. After degeneracy is removed near point B, the core expands and a non-degenerate phase follows with stable helium burning, roughly at the same temperature at which the flash phase had started but at much lower densities. The internal structure of the model after the ignition of helium is indicated in Fig. 33.10.

The calculations by Thomas (1967) were carried out with neutrino rates which turned out to be too high. In calculations for $1.3M_{\odot}$, with more realistic neutrino rates (and composition), the igniting shell was at $m/M = 0.11$, similar to the value in Fig. 33.7, which is based on calculations with the most recent neutrino loss rates. Sweigart and Gross (1978), and more recently Salaris and Cassisi (2005), investigated in detail the dependence of the core mass and the location of the temperature maximum as function of mass, helium content, and metallicity. For

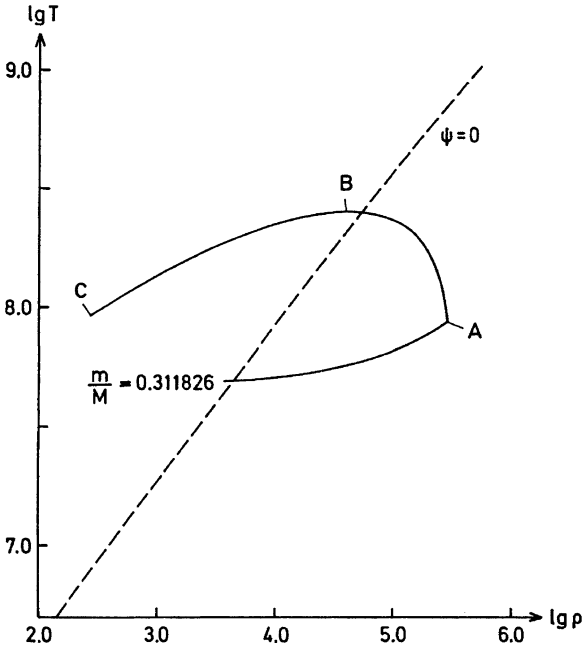

Fig. 33.8 Temperature T (in K) versus density ϱ (in g cm^{-3}) for the mass shell at which helium ignites in the $1.3M_\odot$ model. The letters A–C refer to the corresponding evolutionary slates in Figs. 33.3 and 33.4. The *dashed line* (degeneracy parameter $\psi = 0$ for $\mu_e = 2$) roughly separates the regimes of degeneracy and non-degeneracy of the electron gas (After Thomas 1967)

stellar masses in the range $0.7 \leq M/M_\odot \leq 2.2$ helium ignites at $m/M \approx 0.17$ for $M = 0.7M_\odot$, while with increasing total mass the shell of ignition moves closer to the centre.

The changing luminosity provided by the hydrogen shell and helium burning is displayed in Fig. 33.9. The timescale in this figure changes several times due to the different phases of the flash, which starts very slowly over several 10^5 years (not shown), but accelerates dramatically once $\log L_{\rm He}/L_\odot > 3$. Within a few years $\log L_{\rm He}/L_\odot > 10$, but drops equally fast after the peak. Around this time, when the layers above the flash location begin to expand, the hydrogen shell basically extinguishes due to the drop in temperature, while the total luminosity remains almost constant. In the following 10^5 years the hydrogen shell reignites and L drops as predicted in Sect. 33.4. The flash and the resulting convection heat up the core such that the lower boundary of helium fusion is moving inwards within approximately one million years. In all hydrostatic calculations this progression is connected with small, secondary helium flashes, as can be seen in the figure. When the star finally settles on the horizontal branch, the core, which is now burning helium under non-degenerate conditions, is already enriched in carbon by about 5 %.

Although the properties of the regions in which the flash occurs can change drastically within a few seconds, it seems as if inertia terms can be neglected even in the most violent phases of the flash. Another open question is, how convection behaves during the rapid evolution of the helium flash and whether the ignition of helium and the flash in a shell proceeds in strict spherical symmetry. Such question can only be answered with 2- and 3-dimensional hydrodynamical calculations.

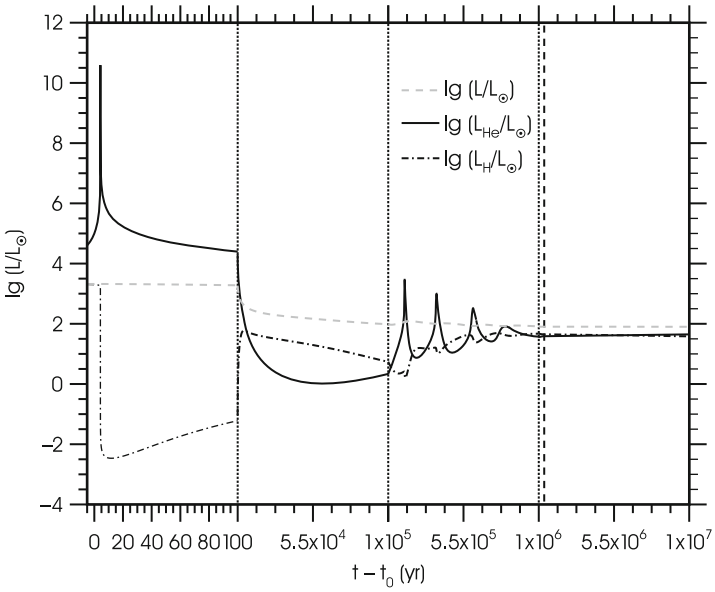

Fig. 33.9 Changes in total (L), hydrogen (L_{H}), and helium (L_{He}) luminosity with time during the helium flash in the 0.85 $M_{\odot}$ star of Fig. 33.5. $t = 0$ is defined for the moment when $L_{\mathrm{He}}/L_{\odot} = 5$, and the zero-age horizontal branch is reached 1.325×10^6 years later. This is defined as the point of minimal total thermal energy and indicated by the *vertical dashed line*. *Vertical dotted lines* delimit ranges of different scale for the time axis

These, however, need such enormous computational resources that so far only parts of stars can be modelled and their evolution be followed for only a short period of a few hours to days. This restricts such simulations to the peak of the helium flash and the inner core of the star. Mocák et al. (2008, 2009) have done such simulations and, apart from some details, confirmed the overall applicability of the 1-dimensional, spherical, and hydrostatic stellar models. However, they seem to predict a much faster heating of the core and the absence of the secondary flashes. This is one of the several unanswered questions connected with the helium flash. Another one is, whether during the flash matter is expelled from the surface.

If helium is ignited off centre, then the burning forms a shell enriched in carbon and oxygen which surrounds a helium sphere. But if the molecular weight decreases in the direction of gravity, the layer is secularly unstable: a mass element pushed down so slowly that it could adjust its pressure and temperature to that of the new surroundings ($DP = 0, DT = 0$, in the terms of Chap. 6) would have a higher density ($D\varrho > 0$, because $D\mu > 0$) and would sink deeper. This corresponds to the "salt finger instability" discussed in Sect. 6.5. In the case discussed here it will cause mixing between the shell in which carbon and oxygen are produced, and the helium region below. The linear stability analysis is rather easy, though it is difficult to follow the instability into the non-linear regime and, for instance, to determine

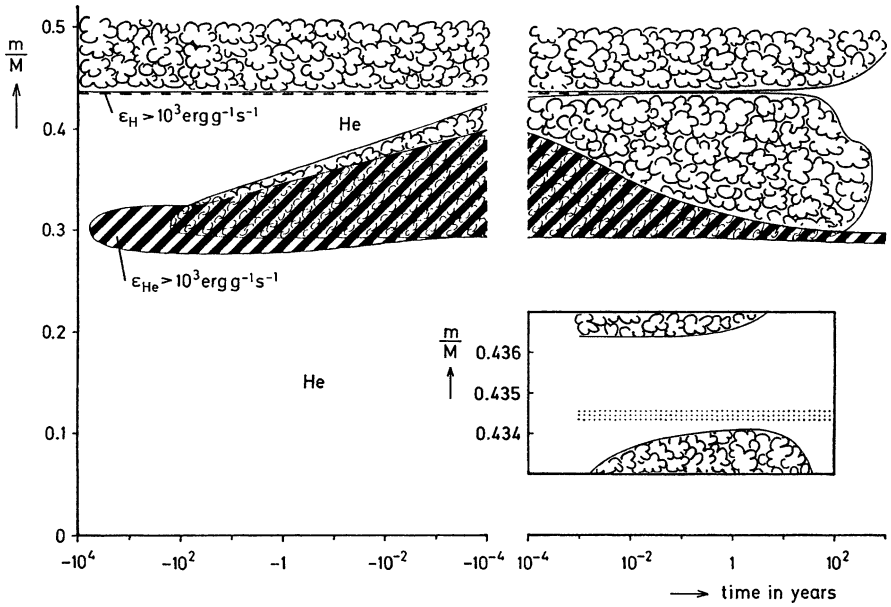

Fig. 33.10 The evolution of the internal structure of a star of $1.3 M_\odot$ during the helium flash. The zero point of the abscissa corresponds to the age 7.474×10^9 years of the abscissa of Fig. 33.4. The main regions of nuclear energy release are hatched; the hydrogen-burning shell is, in the mass scale of the ordinate, so narrow that it appears as a *broken line*. It extinguishes at $t \approx 10^{-3}$ years. "Cloudy" areas indicate convection. The close approach of the outer convective envelope and the convective region above the helium-burning shell is shown with a strongly enlarged ordinate in a window at the *lower right*. There the *dotted area* indicates the transition region of the chemical composition left by the (then extinguished) hydrogen-burning shell

the characteristic time for this mixing process. Simple assumptions about the flow pattern suggest that mixing due to the inwardly decreasing molecular weight is slow compared to the nuclear timescale and can therefore be neglected (Kippenhahn et al. 1980a,b). The multidimensional hydrodynamical models by Mocak and co-workers mentioned above indeed show the occurrence of such fingers, which, however, the authors ascribe to Rayleigh-Taylor instabilities. They could be followed for less than 2 days only.

More spectacular mixing than in the case just discussed can occur if the convective shell, forming above the helium-burning shell during the flash, merges with the outer convective layer. Then hydrogen-rich matter will be mixed down to regions with high temperatures where simultaneous helium and hydrogen burning give rise to quite unusual nuclear reactions and chemical compositions. Although the boundaries between the two convective zones come very close to each other, they do not merge usually. This can be seen in the detailed picture on the lower right of Fig. 33.10. But there are situations where such "flash-induced mixing" indeed happens. The first example is stars with zero initial metallicity, so-called Population III stars, and with $M \lesssim 1.0\, M_\odot$. In such stars only the *pp* chains can

produce helium, and this leads to a different temperature stratification, which allows the penetration of the hydrogen/helium discontinuity by the convective layers above the helium ignition shell (Fujimoto et al. 1990). The result of the flash-induced mixing are surface abundances drastically enhanced in carbon produced by triple-alpha reaction and in nitrogen resulting from proton captures on some of this carbon (Schlattl et al. 2001). The second case where this was encountered is Pop. II stars with extremely thin hydrogen envelopes (of order $10^{-4}\,M_\odot$), which could be the result of enhanced mass loss on the red giant branch (RGB). Due to the low envelope mass the hydrogen shell is extinguishing and the star leaves the RGB, returning first to hotter temperatures and then entering the white dwarf cooling phase. If on its way across the Hertzsprung-Russell diagram the helium flash sets in (such stars are also called "hot flashers"), convection can penetrate into the envelope to engulf protons into the hot helium-burning regions, which leads to a "CNO flash". As a consequence the surface is enriched both in helium and carbon, and the star resembles, both in composition and its location, stars at the very hot end of the horizontal branch (see Sect. 33.6). For more details we refer the reader to Cassisi et al. (2003).

33.6 Evolution After the Helium Flash

After the violent phase of the helium flash there follows a phase of quiet burning in non-degenerate matter. The transition to this is not particularly well covered by calculations; one of the few exceptions is shown in Figs. 33.5 and 33.9. Most authors prefer to start with models that belong to a later state in which the models already resemble the horizontal-branch stars of globular clusters. These methods and how accurately they reproduce the full calculations carried through the complete flash event can be found in Serenelli and Weiss (2005). One should keep in mind, though, that the comparison is done with spherical symmetric, hydrostatic models. Once multidimensional hydrodynamical models are available for all phases of the helium flash, one will see how accurate the hydrostatic models are themselves.

Although during the flash helium is ignited in a shell, it will also burn in the central region after some time, and the stars can be approximated by models on generalized main sequences (cf. Sect. 23.3). For example, a $0.9M_\odot$ star, having a helium core of $0.45\,M_\odot$ after the flash, corresponds to the generalized main sequence for $q_0 = 0.5$. Then from Fig. 23.5 we expect that the model should lie in the HR diagram near the Hayashi line at a luminosity of about $L \approx 100L_\odot$, appreciably lower than just before the flash. This is also what we had expected from the analytic discussion at the end of Sect. 33.4, and the historical evolutionary track in Fig. 33.3 in fact already pointed downwards in the right direction. The modern calculation of Fig. 33.5 covers the whole post-flash part. When in the subsequent phase q_0 increases with growing M_c, the model should cross over to generalized main sequences of larger q_0, i.e. move to the left with slightly increasing luminosity. This also applies when comparing models of the same core, but different total

mass, and therefore different values of q_0. Thus, the analytic discussion and the generalized main sequences already sketch basic properties of the phase following the helium flash, which is identified as the (zero-age) horizontal branch.

Detailed calculations, first carried out by Faulkner (1966) in order to reproduce the horizontal branch of globular clusters, show that the models after the helium flash depend not only on q_0 but also on the chemical composition. He compared models of different mass M in complete equilibrium at the onset of quiet helium burning in a core of $M_c = 0.5 M_\odot$ with a hydrogen-burning shell at the bottom of the envelope. For $M > 0.75\, M_\odot$ (at about solar metallicity) they were close to the Hayashi line, but for a smaller mass, they were located considerably to the left. In order to cover the whole observed horizontal branch with such models for a fixed metallicity, one has to assume that the models differ in mass. In a globular cluster, where all stars have the same age and all stars at the tip of the RGB and on the zero-age horizontal branch (ZAHB) had nearly the same initial mass, the horizontal extent of the horizontal branch provides stringent evidence for different mass loss during the previous phase, either before or during the helium flash. This question still awaits a final answer, but the most likely scenario is the following:

During the slow evolution before the helium flash the stars lose an appreciable, but from star to star different, amount of mass from their surfaces. Then the stars start their evolution after the flash with the same core masses but different envelope masses: those which have lost more mass lie on the left, while those which have lost only little mass lie in the red region (Fig. 33.12).

To some degree, however, the observed horizontal branches reflect the evolution of stars after their appearance on the zero-age branch. When their cores grow owing to shell hydrogen burning, and the helium is consumed in their central part, their evolutionary tracks loop back and forth, populating the horizontal branch. The observed branches are not simply the locus of zero-age models. We will come to the further evolution in Sect. 33.7. Since the horizontal branch crosses the instability strip (see Chap. 41) we can expect pulsating horizontal-branch stars. Indeed there one finds the RR Lyrae variables.

Faulkner's results revealed another important property of zero-age models. If one keeps the total mass constant but decreases their metal content, then the models move to the left of the HR diagram. This helped to understand an observed correlation between horizontal-branch characteristics of different globular clusters and their composition: the concentration of stars on the horizontal branch shifts from left to right with increasing contents of heavier elements. This is usually called the *first parameter* effect for horizontal-branch morphology. Observations point to a *second parameter*, which so far has not been identified undisputedly. There exist pairs of globular clusters of (almost) identical age and the same metallicity, but different numbers of stars on the red and blue part of the horizontal branch. Examples for such famous "twins" are M13 and M3, and NGC 362 and NGC 288. Among the candidates for the second parameter are age, helium content, and the density of stars inside the cluster.

Detailed, full evolutionary calculations confirm all these dependencies. We show in Fig. 33.11 the location of ZAHB models for three different metallicities, ranging

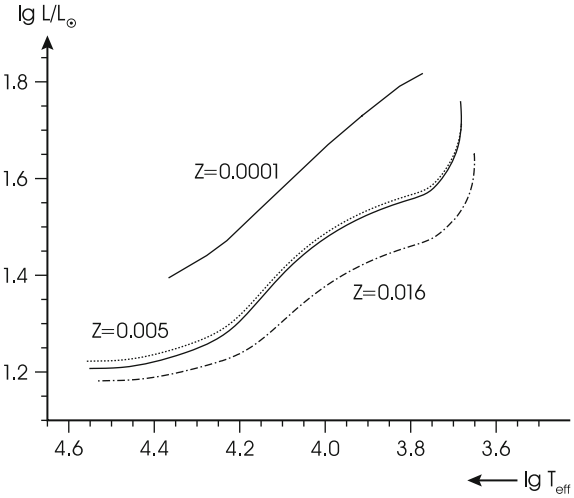

Fig. 33.11 Zero-age horizontal-branch (ZAHB) models for different compositions. The ZAHB brightness increases with decreasing metallicity, which is in this version $Z = 0.016$, 0.005, and 0.0001. The two lines for $Z = 0.005$ correspond to ages of 15 Gyr (*dotted*) and 5 Gyr (*solid*)

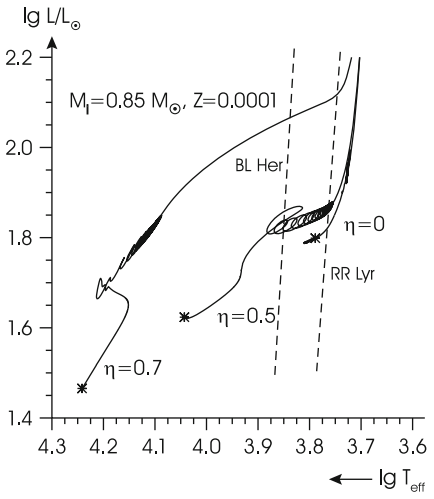

Fig. 33.12 Evolution on the horizontal branch starting at the zero-age position for models with different mass loss rates during the preceding red-giant phase, indicated by the η-parameter in the mass loss formula (9.1). The main-sequence mass was $M_{\rm i} = 0.85 M_{\odot}$ in all cases; at the beginning of the horizontal-branch evolution, the models have 0.85, 0.66, and $0.56 M_{\odot}$ (*right to left*). The *loops* correspond to the so-called "mini pulses". The *dashed lines* indicate the location of the instability strip, continuing that for classical Cepheids (Fig. 31.4). In this strip, the RR Lyr and BL Her variable stars are found; they are obviously stars either in or after the HB phase

from $Z = 0.0001$ to $Z = 0.016$. The lower the metallicity, the brighter the stars on the ZAHB. Along each ZAHB, mass and therefore envelope mass varies. The coolest models were obtained from calculations ignoring mass loss, the hottest ones have only very thin hydrogen envelopes left. For the two more metal-rich cases they were obtained by removing mass from the coolest ZAHB models. This is one of the mentioned approximative ways to construct such models. The ZAHB for $Z = 0.0001$ was taken from calculations that followed the complete evolution from the ZAMS through the core helium flash to the horizontal branch. The zero-age stage was identified with the model having the smallest thermal energies.

In this $\log T_{\rm eff}$-$\log L/L_\odot$ diagram the horizontal branch appears to be "horizontal" only in some $T_{\rm eff}$ regions. This is partly because of the narrow range in luminosity shown, but its appearance in fact also depends a lot on the photometric band it is observed in. However, if extending over the full temperature or colour range, it never is completely horizontal.

The ZAHB for $Z = 0.005$ in Fig. 33.11 appears as a pair. The slightly brighter branch corresponds to an age of 15 Gyr, the other one to one of 5 Gyr. This in turn reflects the slight dependence of the core mass at the helium flash on initial mass: the brighter branch originates from stars below $\approx 1.0\,M_\odot$, the dimmer one from $M \approx 1.3\,M_\odot$.

More details about the dependency of the ZAHB luminosity on core mass, helium content, and metallicity, including quantitative results from theoretical models, can be found in Salaris and Cassisi (2005), Chap. 6.3.

33.7 Evolution from the Zero-Age Horizontal Branch

A so-called ZAHB model has a homogeneous non-degenerate helium core of mass $M_{\rm c} \approx 0.45 - 0.50\,M_\odot$, surrounded by a hydrogen-rich envelope of mass $M_{\rm env} = M - M_{\rm c}$. The total luminosity consists of comparable contributions from (quiet) central helium burning and from the hydrogen-burning shell.

A complication occurs during the following evolution of these models. The stars have a central convective core which becomes enriched in carbon and oxygen during helium burning. The opacity in this temperature-density range is dominated by free-free transitions. However, the free-free opacity increases with increasing carbon and oxygen abundance as can be seen from the factor B in (17.5) and (17.6), which depends on the square of the nuclear charge. As a consequence the radiative gradient inside the Schwarzschild boundary grows during core helium burning, and a discontinuity in $\nabla_{\rm rad}$ at the edge of the convective core develops. The situation is similar to that in massive stars on the main sequence (see Sect. 30.4.2) where the opacity is governed by electron scattering and decreases with increasing helium abundance. In this case the core is therefore shrinking during the main-sequence evolution. The radiative layers of increasing hydrogen content above the core can locally become convective if some mixing increases the hydrogen content (Fig. 30.3).

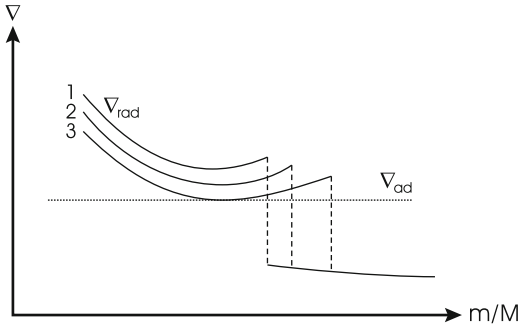

Fig. 33.13 Change in the run of the radiative temperature gradient with time during the evolution on the horizontal branch (see text). Three situations 1–3 for increasing time are sketched (after Salaris and Cassisi 2005)

A similar semiconvective situation is given outside the convective helium-burning core on the horizontal branch. If some mixing, for example, due to overshooting, mixes C/O-enriched material outside the formal Schwarzschild border, the radiative gradient will increase there and convection sets in. Such cores therefore have the tendency to grow, and a jump in $\nabla_{\rm rad}$ at the convective core boundary cannot develop in the early phase of HB evolution. Detailed models show that the radiative gradient then tends to increase and to develop a minimum inside the growing convective core, which, due to the continuing mixing of helium-rich layers and the combined effect of changing physical quantities, at some point begins to become smaller, until it drops to the value of the adiabatic value. This change in the radiative gradient with time is sketched in Fig. 33.13 for three consecutive times. Further mixing at the core border then would lead to a stabilization of an intermediate region, and therefore to the development of a radiative zone inside the core. In real stars one expects therefore mixing up to a composition that leads to a marginally unstable layer with $\nabla_{\rm rad} = \nabla_{\rm ad}$. This partially mixed layer constitutes another case of semiconvection, and was discussed first by Castellani et al. (1971). The development of this situation is indicated by the line labelled "3" in Fig. 33.13, and the real situation in a stellar model calculated with semiconvection is shown in Figs. 33.15 and 33.16.

If a continuous, slow growth of the convective core is inhibited, a strong discontinuity at its edge is developing. As in the case of massive stars, during the further evolution, a sudden mixing between the core and the overlying, helium-rich layers may occur, which leads to a sudden increase in the core's helium content and a loop in the HR diagram. The occurrence of these so-called "breathing pulses" depends a lot on the details of the treatment of convection and of the border of the convective core. The most favourable situation for their occurrence is when the Schwarzschild criterion for convection is used, but they are probably an artefact of the calculations (see the discussion in Salaris and Cassisi 2005). In most of the models we show in Figs. 33.12 and 33.14 they are not present.

Figure 33.14 shows evolutionary tracks for the horizontal-branch evolution of the same initial pre-ZAHB model with $M = 0.6856\,M_\odot$ ($Z = 0.0001$), calculated with either the Schwarzschild criterion for convection (solid line), the Ledoux criterion and semiconvection (dotted line), or with overshooting (dashed line). The

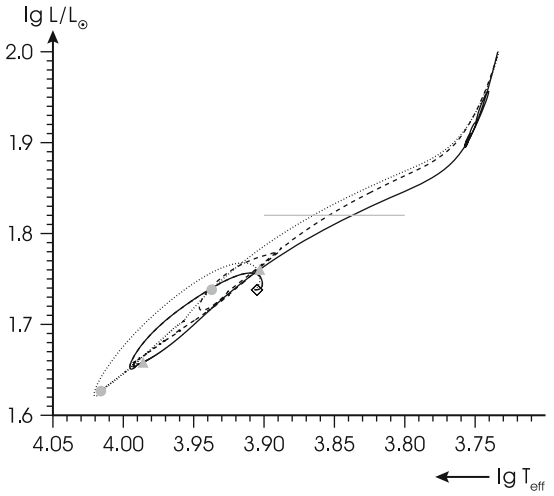

Fig. 33.14 An example for horizontal-branch evolution using different treatments for convection. The evolution begins at a pre-ZAHB position (*diamond symbol*) for a mass of $0.6856\,M_{\odot}$ ($Z = 0.0001$). The *grey triangles* and *circles* refer to models used for Fig. 33.16. *Solid line*: Schwarzschild criterion; *dashed*: Schwarzschild and overshooting; *dotted*: Ledoux criterion and semiconvection. The *horizontal line* indicates where the interior hydrogen profile of the models of Fig. 33.15 was taken

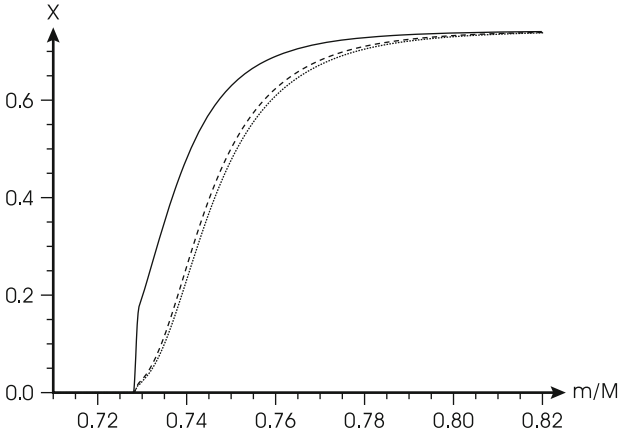

Fig. 33.15 The hydrogen profile in three horizontal-branch models taken from the tracks of Fig. 33.14, taken at approximately the same luminosity. The linestyles refer to the same cases as in the previous figures

overshooting model initially follows the track of the Schwarzschild case, until after the hottest point on the evolution the core is expanding; generally higher luminosities are reached, but also a second loop close to the initial ZAHB position takes place. After this the track with overshooting is slowly approaching the one

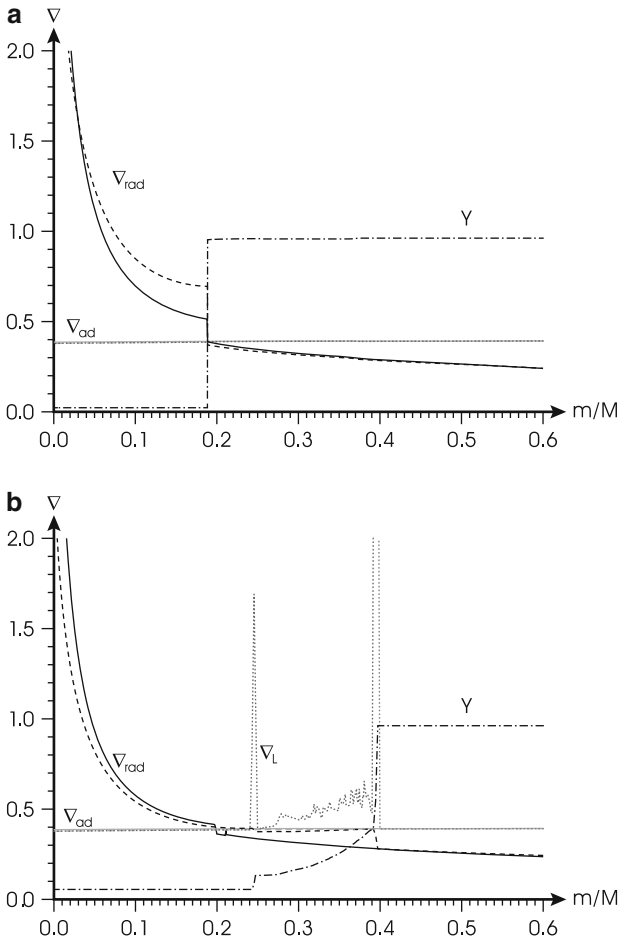

Fig. 33.16 (**a**) The radiative (*black lines*) and adiabatic (*grey lines*) temperature gradients in two models of Fig. 33.14, indicated there by *triangles*, calculated with the Schwarzschild criterion. The *solid line* refers to a state at the beginning and the *dashed line* to the end of horizontal-branch evolution. The *dash-dotted line* shows the helium mass fraction in the latter model. (**b**) The same for the case using the Ledoux criterion and semiconvection. The two models are indicated by *circles* in Fig. 33.14. Additionally, the Ledoux-gradient ∇_{L} (6.12) is shown as the *grey dotted line*. Notice the fact that ∇_{rad} is almost identical to ∇_{ad} as the result of semiconvective mixing

calculated with semiconvection. In this latter case, only one extended loop takes place in the final phase of approaching the ZAHB (which here can be identified with the hottest point on the track), and then the evolution is proceeding smoothly to higher luminosities and cooler temperatures. In Fig. 33.15 we show the run of hydrogen abundance inside models taken at approximately the same luminosity of $\log L/L_{\odot} = 1.82$. The composition jump at the edge of the convective core

is clearly visible for the Schwarzschild case, as is the similarity between the overshooting and semiconvection model in this late phase of the HB evolution.

The mass of the helium core grows owing to hydrogen-shell burning, while in the convective core helium is consumed and carbon and oxygen are produced. After some time a pure carbon-oxygen core will be formed in the central region of the helium core. Then nuclear burning takes place in two shells (hydrogen and helium burning), and in the subsequent phases of evolution, the masses below these shells will grow.

The models evolve from the ZAHB first in the slow phase of central helium burning with a hydrogen-burning shell. This phase, which lasts for several 10^7 to up to 10^8 years, is followed by a phase of rapid evolution during which the models go from helium burning in the centre to shell burning. In this phase another kind of loops appears, which is clearly visible in Fig. 33.12; these are the so-called "mini-pulses", which were described early on by Mazzitelli and D'Antona (1986). The steep chemical profile of models calculated with the Schwarzschild criterion (Fig. 33.15) leads to a thinner helium shell; such shells can be thermally unstable. We will discuss such shell instabilities in more detail in Chap. 34. After this initial shell-burning phase a slow phase of double shell burning occurs.

The general direction of the evolution is towards higher luminosity and a return to the Hayashi line. Depending on the relative energy production of helium core and hydrogen shell the models initially show more or less extended excursions towards higher $T_{\rm eff}$ (see the model with the lowest mass compared to the coolest one in Fig. 33.12).

The evolutionary tracks lead upwards with increasing core mass, and the corresponding branch in the HR diagram is called the *asymptotic giant branch* (AGB). It has to be distinguished from the *red giant branch* (RGB), along which the image points in the HR diagram move upwards *before* ignition of helium. The models of the post-horizontal-branch evolution occupy a region above the horizontal branch. During their evolution some of them cross the instability strip (see Chap. 41), where one finds the pulsating BL Herculis[1] stars (compare the sketch in Fig. 33.12). In contrast, the RR Lyrae variables are stars, which are still on the horizontal branch, and which are located in the region, where it crosses the instability strip.

[1]BL Her stars belong to the class of *type II Cepheids*, which used to be called collectively W Virginis stars. Nowadays the latter term is used for even brighter stars in the same instability strip, which cross it during an excursion from the AGB.